

Contents list available at CBIORE journal website

Remarkable Energy Development

Journal homepage: https://ijred.cbiore.id



Research Article

Energy harvesting through the triboelectric nanogenerator (TENG) based on polyurethane/cellulose nanocrystal

Jose Miguel Blancas-Flores ^{a.}, Juan Morales-Rivera ^{a.}, Gilberto Rocha-Ortiz ^{a.}, Irán Fernandez Hernandez Ahuactzi ^{a.}, José Jesus Cabrera-Chavarria ^{a.}, Hugo Armando Andrade-Melecio ^{b.}, Pablo Daniel Astudillo-Sanchez ^{a.}, Víctor Hugo Antolín-Cerón ^{a.}

Abstract. This study investigates how physical and mechanical properties affect the performance of triboelectric nanogenerators (TENGs). Polyurethane (PU) was prepared using two methods: (i) one-step PU (non-chain extended polyurethane) and (ii) two-step PU (chain extended polyurethane) via the prepolymer method; both types were filled with different concentrations of nanocrystalline cellulose. Mechanical properties significantly influence the deformation at the material interface that occurs during contact or friction. Key surface characteristics, including surface energy, geometry, and physicochemical properties, affect the effective contact area and potential distribution. One-step PU with 0.1 % CNC demonstrates a maximum capacitance of 29.20 pF, a voltage of 2.04 V, an electric current of 0.43 μA and power of 0.89 μW, representing a 74.5 % increase in power compared to the neat one-step PU, exhibits significant potential for TENG applications. Performance improvements are associated with lower concentrations of cellulose nanocrystals, enhanced hydrogen bonding, and beneficial surface energy. The observed enhancements in output are attributed to improved internal polarization from well-dispersed crystalline nanocellulose, increased crystallinity of the soft segment, and reduced charge transfer mechanisms due to amino groups in the chain extender. However, the impact of the molecular structure and conformation of polyurethanes on triboelectrification remains unclear, highlighting the need for theoretical models and experimental data. This research provides a practical approach for developing stretchable triboelectric materials with enhanced mechanical properties to optimize TENG design.

Keywords: Energy harvesting, Polyurethane, cellulose nanocrystal, Nanocomposites, Triboelectric nanogenerator,.



@The author(s). Published by CBIORE. This is an open access article under the CC BY-SA license (http://creativecommons.org/licenses/by-sa/4.0/).

Received: 9th Sept 2024; Revised: 29th Oct 2024; Accepted: 6th Nov 2024; Available online: 11 Nov 2024

1. Introduction

TENG (triboelectric nanogenerator) performance, among other properties, primarily depends on the interfacial interactions of materials and charge generation at the contact layers. Modifying surface morphology has been introduced as an effective method for enhancing TENG performance (Wang et al., 2021). This can be achieved through chemical modification of surfaces to improve the materials' tendency to gain or lose electrons during interactions with other materials (Yu et al., 2016). Many authors have focused on finding the optimal combination of materials to maximize charge generation, along with surface modifications such as pore structures to increase contact area. However, few have explored the relationship between electrical response and the physical and chemical properties of the materials used. There is a substantial need to understand and develop advanced, high-performance materials to enhance the output power of TENG systems. TENG performance depends on various factors, among the most important are: (i) interfacial interactions of materials and charge generation on the contact layers, (ii) surface morphology

modifications, and (iii) chemical modifications (Shen et al., 2017). Adding nanofibers to elaborate nanocomposites is one method of chemical modification (Mi et al., 2018). Several materials are used to develop TENG nanogenerators, including natural rubber (Bunriw et al., 2021), polytetrafluoroethylene (PTFE), polyetheretherketone (PEEK), polyphenylene sulfide (PPS), polyethylene terephthalate (PET), pluorinated ethylene propylene (FEP), poly(vinylidene fluoride) (PVDF), polyvinyl chloride (PVC), nylon (PA), polycarbonate (PC), polyetherimide (PEI), polypropylene (PP), polyethylene (PE), polyimide (PI), poly(styrene) (PS), Nitrile, polydimethylsiloxane (PDMS) (Zhao et al., 2021; Zhang et al., 2020). On the other hand, polyurethane has been studied by some authors (Lee et al., 2015; Zheng et al., 2021) who have explored the output response of PU and modifications such as introducing porous structures and incorporating nanoparticles like CNTs, Au, Fe, or self-healable materials (Sun et al., 2018). Wang et al. provided an extensive list of triboelectric materials and suggested effective pairings. They also offered important theoretical insights, which have contributed to understanding different modes of triboelectric operation (Zou et al., 2019). Therefore, selecting the appropriate

Email: victor.antolin@academicos.udg.mx (V. H. Antolín-Cerón)

^aDepartamento de Ciencias Básicas Aplicadas, Universidad de Guadalajara, Tonalá 45425, México

^bDepartamento de Ingeniería Química, Centro Universitario de Ciencias Exactas e Ingenierías, Universidad de Guadalajara, 44430, México

^{*} Correspondence author

materials is crucial for maximizing charge generation in the development of TENG devices (Wang et al., 2017; Fan et al., 2012). Thermoplastic polyurethane (TPU) materials have advantages such as flexibility, low cost, processability, market availability, and their use in sportswear textiles, like Lycra or Spandex®. Additionally, incorporating nanocellulose crystals into TPU introduces a large number of oxygen atoms into the cellulose, which tends to lose electrons and can induce a slightly positive charge in triboelectric devices (Yao et al., 2016; Yao et al., 2017). Therefore, they are commonly used as positive triboelectric nanofillers in TENGs (Vatankhak et al., 2021). Additionally, the nanometer size of nanocellulose provides properties such as excellent strength and stiffness, as well as a high surface area, which enhances the overall properties of the nanocomposite. It is important to note that during the triboelectric process, polymeric materials can experience irreversible wear and failure, which can reduce energy conversion efficiency and limit practical applications. Consequently, it is essential to modify and fabricate TENG devices with mechanically enhanced properties (Niu et al., 2018). In this context, employing nanostructured fillers in TENG devices could effectively address these challenges. However, it remains unclear how the polymer chain structure of PU influences the triboelectrification process. Several questions arise, such as: What is the effect of the degree of phase separation between the soft and hard segments? Does hydrogen bonding influence or enhance the triboelectric response in PU? Is the use of a chain extender appropriate? Do nanofillers contribute to electric charge? These and others questions related to the physical and chemical properties studied in this work are explored to better understand TENG devices.

Previously, we reported on the use of PU nanocomposites with CNC, exploring their application in creating membranes for protein separation (Antolin *et al.*, 2022). These membranes demonstrated high mechanical performance, making them suitable for use in triboelectric devices. Although there are a few reports correlating chemical structure with output response in TENGs, it remains uncertain how the intrinsic properties of PU, such as hydrogen bonding, mechanical properties, surface energy, and crystallinity, affect triboelectric behavior in these materials. In this work, we identified a set of considerations that determine whether the properties of hard or soft segments are suitable for fabricating PU TENGs.

2. Methodology

2.1 Materials

Poly(1,4 butylene adipate) (Diexter G 4400-57) with a hydroxyl equivalent weight of 984 was supplied by Coim USA Inc. (West Deptford, NJ, USA), isophorone diisocyanate (IPDI), Hexamethylene diamine, Tin (II) 2-ethyl hexanoate and *N,N* dimethyl formamide (DMF) ethylenediamine were acquired from Aldrich. Dichloroethane and absolute were purchased from Merck (Naucalpan, México), and chloroform 99.8 % from Karal México, All reagents were dried before being used

2.2 Synthesis of Cellulose Nanocrystal

CNCs were prepared by the acid hydrolysis of commercial cellulose microcrystals (MCCs), following a method reported in the literature (Cranston et al., 2006; Fortunati et al., 2012; Navarro et al., 2014). First, 20 g of MCC and 175 mL of sulfuric acid solution (64 % (w/w)) were mixed in a 250 mL three-neck round-bottom flask and homogenized with a mechanical stirrer. Hydrolysis was carried out at 45 °C for 30 min. The resulting product was diluted in 4 L of deionized water to stop the hydrolysis reaction. Next, to remove excess acid, the suspension was centrifuged, yielding 1 L of CNC suspension. The suspension was then dialyzed for 5 days to achieve neutralization. To purify the suspension, ion exchange resin (Dowex Marathon MR-3 in hydrogen and hydroxide form) was added and stirred for 24 h, then removed by filtration. The pH of the CNC suspension was adjusted to around 9.0 by adding a 1.0 % NaOH aqueous solution dropwise while stirring (Arrieta et al., 2016). The CNC suspension was then sonicated to obtain a stable suspension of the nanocrystals and stored in a refrigerator at 3 °C to prevent bacterial growth.

2.3 Synthesis of PU and their Nanocomposites

One-step PU were elaborate mixing Diexter diol (2.5 g) and IPDI (0.57 g) with a equimolar ratio (OH:NCO = 1:1) with 25 mL of 1,2-dichloroethane (see figure 1) into a flat bottom flask. Then, the catalyst, stannous 2-ethylhexanoate (Tin II) (1:100 mol by diol moles), was added and stirred vigorously for 6 h at 80 $^{\circ}$ C. The resulting polymer solution was poured over a

$$\begin{array}{c} \mathbf{a} \\ \\ \mathbf{b} \\ \mathbf{2} \\ \\ \mathbf{O} \in \mathbb{C}^{2N} \\ \\ \mathbf{N} = \mathbb{C} = \mathbb{O} \end{array} \\ \begin{array}{c} \mathbf{h} \\ \\ \mathbf{Poly(butylene \ adipate)} \\ \mathbf{h} \\ \\ \mathbf{Poly(butylene \ adipate)} \\ \mathbf{h} \\ \\ \mathbf{h} \\ \mathbf{$$

Fig 1. Chemical pathway of: a) for one-step, and b) two-step polyurethanes

Teflon mold and kept at ambient temperature for 36 hours to evaporate the excess of solvent.

Two-step PU (prepolymer method). Dry polyester diol and isophorone diisocyanate (OH:NCO mol ratio 1:2) were added to a 100 mL round-bottom flask, which already contained a solution of 1,2 dichloroethane (25 mL) and stannous 2-ethylhexanoate as the catalyst (18 $\mu L,\,0.055$ mmol). The mixture was stirred for 3 h at 80 °C. Then, the chain extender (HMDA, 0.15 g, 2.58 meq with 2 mL of N,N dimethyl formamide) was added dropwise. The reaction mixture was maintained at the same temperature for 3 h.

For nanocomposite synthesis, specific amount of CNC (0.1, 0.5, 1, and 2 % wt) were added to the initial solution of polyester diol and IPDI in 1,2 dichloroethane, and this mixture was sonicated for 15 min. Then the catalyst was added, and the reaction mixture was heated at 80 °C under stirring for 3 h. and the same procedure was followed for both one-step and two-step PU. The product was poured into a leveled Teflon mold and allowed to set at room temperature for 24 h. Solvent evaporation continued for 36 hours until a film was obtained. The film was then removed and dried in a vacuum at room temperature for 12 hours.

2.4 Differential Scanning Calorimetry (DSC)

DSC was used to study the thermal properties of the prepared nanocomposites. The measurements were carried out on a Mettler Toledo DSC model DSC822e previously calibrated with indium. All tests were performed under a nitrogen atmosphere. Thermograms were recorded by heating the samples from -90 to $80\,^{\circ}\text{C}$ at $10\,^{\circ}\text{C/min};$ only the second scan was reported. Sample weights ranged between 5 and 10 mg. The glass transition temperature (Tg) of the polymer matrix was evaluated by the inflection point criteria and the melting enthalpy was calculated from the area under the endothermic peak.

2.5 Mechanical Test

Tensile stress–strain tests were conducted at a deformation rate of 50 mm/min using a United Model SFM-10 machine. The samples tested were rectangular prisms with dimensions $55 \times 12 \times 0.5$ mm in accordance with the ASTM D882 standard test method. Five samples were tested for each polymer composition. In addition, it is essential to investigate the inherent relationship between hardness and elastic modulus in soft materials, such as polyurethanes. Several investigations have explored the connection between the elastic modulus and hardness of soft materials, based on the Gent's theory (Gent et al., 1958).

$$E = \frac{0.0981(56+7.66S_A)}{0.137505(254-2.5S_A)} \tag{1}$$

According to Ruess's study, the linear relationship between hardness and material elastic modulus is given by: (Bakošová *et al.*, 2022).

$$Log_{10}E = 0.0235S_A - 0.6403 (2)$$

where S_A refers to the ASTM D2240 type A shore hardness, and E refers to Young's modulus in MPa.

2.6 Infrared Spectroscopy (FTIR)

FTIR spectra of CNC, PU, and the nanocomposites were obtained using an Alpha II spectrophotometer from Bruker with an attenuated total reflection (ATR) unit. Each spectrum represents an average of four scans with a resolution of 2 cm⁻¹. Additionally, the degree of carbonyl groups participating in hydrogen bonding for one-step PU can be estimated using the carbonyl hydrogen bonding index, *R*, as defined by equations 3. Equation 4 was the used to calculate the degree of phase separation (DPS). Finally, equation 5 was used for calculate DPS of the two-step PU.

$$R = \frac{c_{bonded} \varepsilon_{bonded}}{c_{free} \varepsilon_{free}} = \frac{A_{1680}}{A_{1720}}$$
 (3)

$$DPS = \frac{R}{R+1} \tag{4}$$

$$DPS = \frac{A_{1645} + A_{1680}}{A_{1645} + A_{1680} + A_{1670} + A_{1720}} = \frac{A_{bonded}}{A_{bonded} + A_{free}} \tag{5}$$

Where A represents the intensity of the characteristic absorbance, C_{bonded} , C_{free} , ε_{bonded} and ε_{free} are the concentration and extinction coefficients of the bonded and the free carbonyl groups, respectively. The ratio $\varepsilon_{bonded}/\varepsilon_{free}$ ranges from 1.0 to 1.2 (Pimentel *et al.*, 1960).

2.7 Determination of Surface energy by contact angle measurement

Measuring contact angle and surface energy provides a better understanding of interactions between solids and liquids. These interactions play a key role in understanding adhesion, material wettability, and biocompatibility, particularly between PU and copper foil (conductive terminals).

The surface energies of solids can be determined by measuring the contact angle between the solid surface and liquids with known surface tensions. The equilibrium forces at the edge of a resting drop can be described by the interfacial energies of the surfaces involved using the Owens-Wendt method (Cranston *et al.*, 2006), from the equilibrium of these forces; both the surface energy and the interfacial tension can be obtained:

$$\frac{\sigma_l(1+\cos\theta)}{2} = (\sigma_L^D \sigma_S^D)^{1/2} + (\sigma_L^P \sigma_S^P)^{1/2}$$
 (6)

Where σ_L^D and σ_L^P represent the dispersive and polar part of the liquid, respectively, while σ_S^D and σ_S^P denote the corresponding contributions from the solid surface.

Owens, Wendt, Rabel, and Kaelble observed that interfacial tension consists of two components, considering the interactions between molecules. Based on their studies, they concluded that there are two main types of interactions: polar and dispersive. Polar interactions include Coulomb interactions between permanent dipoles, as well as interactions between permanent and induced dipoles. Dispersive interactions arise from the time-dependent fluctuations of charge distributions within molecules. The combination of these contributions determines the surface energy and surface tension of solids and liquids, respectively.

In this work, the surface energies of urethanes and copper foil were evaluated by measuring static contact angle (θ) with a smartphone camera for comparison. The tests were conducted on the air-facing surfaces of the samples using four liquids: water, formamide, ethylene glycol, and glycerol applying the

sessile drop method (Owens *et al.*, 1969). Thus, the contact angles were measured with two of these liquids, resulting in two equations in the form of equation 6, each with different values of the constant coefficients. This procedure yields a system of two linear equations:

$$y_1 = ax_1 + b, y_2 = ax_2 + b (7)$$

$$y_i = \frac{(1+\cos\theta)}{2} \frac{\sigma_L}{\sqrt{\sigma_L^D}}; a = \sqrt{\sigma_S^P}; x_i = \sqrt{\frac{\sigma_L^P}{\sigma_L^D}} \text{ and } b = \sqrt{\sigma_S^D}$$
 (8)

Where x_i and y_i are the contact angle values for the two measuring liquids, a and b are the coefficients dependent on the kinds of these liquids. Then the solution of the system of equations (7 and 8) will determine σ_S^D and σ_S^D components.

2.8 Design and testing of triboelectric nanogenerator

The PU nanocomposite films were assembled into a vertical contact-separation configuration TENG. They were placed on a 2×2 cm copper foil at the base of the vibration exciter a force of 4 N and a frequency of 23 Hz and covered with an additional copper foil on top. Conductive wires were attached to both copper foils to enable electrical measurements. The films underwent a series of press-and-release cycles, with vertical movements of up to 5.5 mm, the electrical characterization was performed with an oscilloscope (UNI-T UTD4204C). Voltage and current values were obtained by averaging the peak-voltage and peak-current measurements, respectively.

The capacitance was measured using an LCR meter (UNI-T UT612) at a frequency of 100 KHz. The PU samples were placed between copper foils, effectively creating a parallel plate capacitor. The dielectric constant was then calculated using equation 9 (Zenkiewicz *et al.*, 2007), where $\boldsymbol{\mathcal{C}}$ represents the capacitance, $\boldsymbol{\varepsilon_0}$ and $\boldsymbol{\varepsilon_r}$ are the dielectric constants of free space and relative, respectively, $\boldsymbol{\mathcal{S}}$ is the area of the copper foils, and $\boldsymbol{\mathcal{d}}$ is the thickness of the PU samples, with had an average thickness of 0.30 mm.

$$C = \frac{\varepsilon_0 \varepsilon_r S}{d} \tag{9}$$

3. Results and Discussion

3.1 Infrared spectroscopy

FTIR spectra of nanocomposites prepared at different CNC concentrations reveal that the addition of CNC affects the peak patterns observed in both families of PU. The FTIR spectra of neat PU and its nanocomposites are shown in Figure 2, with expanded views of the carbonyl (Figure 2a) and amine (Figure 2b) regions. The ester carbonyl band of the pure PU is centered at around 1720 cm-1. In the nanocomposites, two main differences are observed: (i) the ester carbonyl band shifts slightly to higher frequencies, and (ii) a shoulder appears around 1680 cm⁻¹. These changes suggest that the carbonyl groups in the PU matrix are more associated through hydrogen bonds in the nanocomposites. A Gaussian deconvolution analysis was conducted to assess the contributions to the ester carbonyl absorption. The carbonyl bands of both pure PU and the nanocomposites were normalized before analysis. Also, as mentioned above, the carbonyl hydrogen bonding index, R, was estimated using equations 3, while the DPS of the one-step PU was calculated using equation 4.

Equation 5 is used to calculate DPS in two-step PU, where urea moieties are divided into three spectral contributions: (i) free urea at 1670 cm $^{-1}$, (ii) H-bonded at 1645 cm $^{-1}$ and carboxylic acid groups (free at 1720 cm $^{-1}$, H-bonded 1700 cm $^{-1}$). DPS is calculated using the absorbance of hydrogen bonded carbonyl groups (absorbance at 1700, and 1645 cm $^{-1}$), and free carbonyl groups (Absorbance at 1730, 1720 cm $^{-1}$ and 1670 cm $^{-1}$). Where A_{bonded} is the absorbance of a hydrogen bonded carbonyl group ($A_{1700} + A_{1645}$), A_{free} is the absorbance of a free carbonyl group ($A_{1730} + A_{1720} + A_{1670}$) (Chuang $et\ al.$, 2021).

The relationship between the structure and triboelectric properties of PUs can be attributed to hydrogen bonding. Figure 2 shows partial IR spectra of both families of nanocomposites,

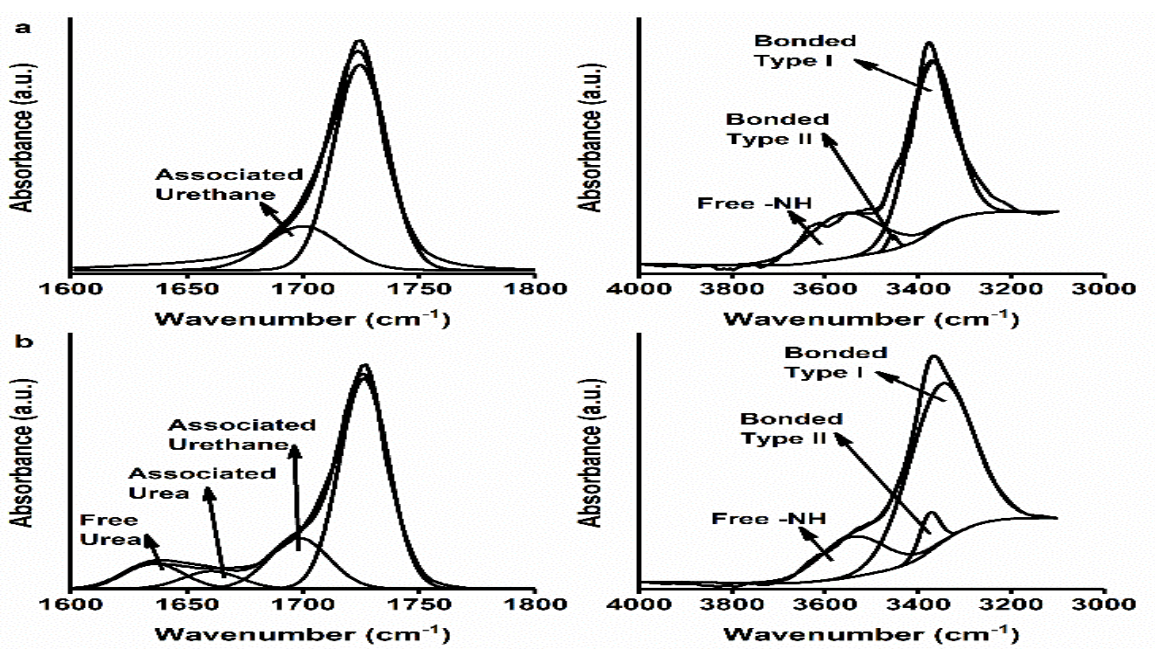


Fig 2. Partial infrared spectral contributions of the carbonyl and -NH regions of a) one-step PU (upper) and b) two-step PU (lower).

Table 1DPS of one-step PU, two-step PU, and their nanocomposites.

Sample	One-step PU	Two-step PU		
	DP	DPS		
Neat PU	15.82	28.69		
PU 0.1 %	21.69	30.36		
PU 0.5 %	19.20	27.15		
PU 1 %	18.22	20.24		
PU 2 %	17.85	26.21		

highlighting the characteristic peaks in the carbonyl and -NH region groups. For one-step PU materials (Figure 2a), a single hydrogen bonding contribution is evident around 1680 cm⁻¹, corresponding to the urethane groups. In contrast, two-step PU materials exhibit a similar hydrogen bonding contribution, but they also show an additional peak at 1630 cm⁻¹ due to the formation of urea groups. This peak indicates additional hydrogen bonding contribution form the formation of bidentate urea associations (Fernandez et al., 1997). The deconvoluted -NH region shows bands attributable to free -NH, hydrogen bonded type I (-NH....O=C), and hydrogen bonded type II (-NH...O-C-ester), respectively. In this region, the peaks for twostep PU are shifted to lower frequencies and exhibit broader bands compared to one-step PU (Ourique et al., 2019). This shift indicates that two-step PU has a greater hydrogen bonding contribution due to the formation of urea bonds and the broader band associated with hydrogen bonding between hard segments. The presence of more hydrogen bonding interactions is evident from the bands, where a higher hard segment content correlates with increased hydrogen bonding. To understand the role of hydrogen bonding in triboelectric devices, Ning et al report that the disruption of hydrogen bonding enhances the dipole polarizability and thus dielectric constant in thermoplastic PU, in this sense one-step PU contains less hydrogen bonding than two-step PU and one-step PU could have better performance in triboelectrification than two-step PU (Ning et al., 2017).

Table 1 shows the degree phase separation (DPS) calculated using equations 3, 4, and 5 for both families of PU and their nanocomposites. The two-step family of PU has larger values of hydrogen bonding contribution compared to the onestep PU. Also, the incorporation of CNC increases the DPS in one-step PU, and conversely DPS diminished in two-step PU nanocomposites. The increase of content CNC favors simple chain structures in one-step PU. In contrast, the presence of CNC in two-step PU implies a disorder in chain folding. CNC can serve as an effective conductive filler to enhance the dielectric constant of the PU matrix, utilizing mechanisms similar to those employed by high dielectric fillers (Jin et al., 2020). On the other hand, it has been demonstrated that stronger hydrogen bonds can form between the N-H group of PU and the free hydroxyl group of CNC, this can lead to the disruption of hydrogen bonds within the PU chains, this fact could be affected in two-step PU since DPS decrease in their nanocomposites (Mattia et al., 2007).

The introduction of CNC into two-step PU reduces interactions among PU chains, promotes the migration of polarized groups, and enhances the polarization ability of PU chains. Additionally, as CNC content increases, the number of free C=O groups in PU rise, while the number of hydrogen-bonded C=O groups decrease due to the formation of hydrogen-bonds between PU and CNC (Kim *et al* 2023, Guo *et al.*, 2023). In the case of one-step PU, the ratio of free C=O bands to hydrogen-bonded C=O bands detected from the FTIR spectra increases as the CNC content rises. According to Table 1, The

peak-area ratio (free C=O bands to hydrogen-bonded C=O bands) increases from 15 to 21 as the CNC content grows from 0 % to 0.1 % wt, As expected, the addition of CNC slightly enhances the permittivity of the PU nanocomposite due to the partial increase in free charge polarization in the PU-CNC interface (Sung *et al.*, 1977).

3.2 Differential scanning calorimetry (DSC)

Figure 3 clearly shows the differing structural behaviors between the two polyurethane families. The one-step PUs exhibit both exothermic and endothermic peaks, indicating their ability to form crystals. In contrast, the two-step PUs shows amorphous behavior with no tendency to crystallize. For both PU families, the glass transition temperature (Tg) of the nanocomposites remains unchanged at -49 °C for one-step PU and -52 °C for two-step PU. Figure 3a shows the impact of CNC on the nanocomposite, evident from the increased enthalpy of fusion in the one-step PU nanocomposite. Figure 3b shows a slight decrease in heat flux for the two-step PU around 20 °C, likely due to the appearance of the Tg of the hard segment, which shifts from 17 to 25 °C with CNC incorporation, suggesting an interaction with the hard segment of the two-step PU. CNC significantly influences the one-step PU by increasing its crystallinity. Crystallinity is an important factor in designing triboelectric generation, as some authors found that crystallinity in the polymer is associated with triboelectric output (Margaronis et al., 2021, Smith et al., 2020).

Based on the DSC data presented in Table 2, one-step PUs could experience significant changes in morphology during the triboelectrification process because their crystallization and melting temperatures are close to room temperature (which is encountered during triboelectrification). While, two-step PUs may show higher mechanical stiffness due to the increased Tg of the hard segment. When environmental temperatures approach the crystallization (Tc) or melting temperatures (Tm) of the macrodiol in a shape fixed material, the morphology may be substantially altered towards a pre-determined shape (Saralegi *et al.*, 2013).

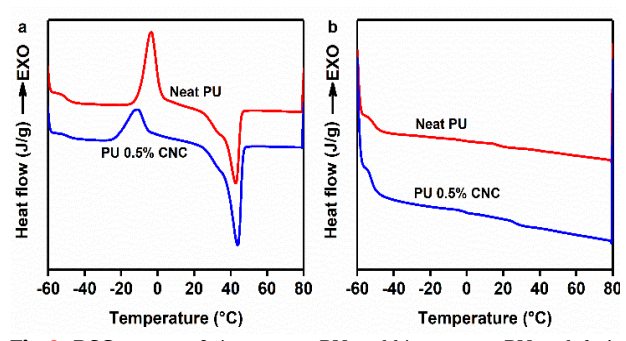


Fig 3. DSC curves of a) one-step PU and b) two-step PU and their nanocomposites (0.5 % wt CNC).

Table 2Data obtained from the DSC curves of PU and their nanocomposites.

Sample	Tg (°C)	Tc (°C)	ΔHc (J/ g)	Tm (°C)	ΔHm (J/g)
		One-st	ep PU		
Neat PU	-49	-4	30	43	37
PU 0.5 %	-49	-10	16	44	41
		Two-st	ep PU		
Neat PU	-52	-	-	-	-
PU 0.5 %	-52	=	_	=	_

Table 3

Mechanical parameter from the stress- strain curves of neat PU and its nanocomposites.

Sample	Young modulus	Yield point (MPa)	Ultimate strength	Strain at break	Toughness
	(Mpa)		(MPa)	(%)	(J/m^3)
		One-step	PU		
Neat PU	6.7 ± 0.5	0.4 ± 0.04	1.40 ± 0.09	751 ± 73	4.3 ± 0.3
PU 0.1 %	23.3 ± 0.8	1.4 ± 0.10	3.02 ± 0.28	611 ± 60	12.5 ± 0.4
PU 0.5 %	58.8 ± 4.1	5.4 ± 0.53	9.30 ± 0.68	350 ± 25	41.1 ± 2.4
PU 1 %	184.1 ± 13	5.8 ± 0.16	7.61 ± 0.61	325 ± 11	9.4 ± 21.7
PU 2 %	163.1 ± 6.8	6.7 ± 0.23	6.90 ± 0.52	129 ± 8	8.1 ± 0.5
		Two-step	p PU		
Neat PU	16.7 ± 0.6	0.6 ± 0.03	3.96 ± 0.12	756 ± 46	12.93 ± 1.0
PU 0.1 %	29.5 ± 1.9	2.8 ± 0.10	9.85 ± 0.74	591 ± 37	60.81 ± 3.6
PU 0.5 %	38.4 ± 2.2	2.2 ± 0.14	17.81 ± 1.58	565 ± 54	47.68 ± 3.0
PU 1 %	176.3 ± 17.2	7.2 ± 0.48	14.32 ± 0.57	483 ± 33	43.35 ± 3.2
PU 2 %	342.2±11.9	7.0 ± 0.18	7.01±0.60	5.2±0.4	0.27±0.01

3.3 Mechanical properties

Figure 4 shows the stress-strain curves of both families of PU. The initial slope of these curves indicates the typical behavior used to calculate Young's modulus. An increase in this slope suggests higher crystallinity, as the crystal content is influenced by the soft segment in PU. Additionally, higher CNC content leads to increased values of Young's modulus for both PU families. Similarly, the yield point also shows a corresponding increase with CNC content, indicating greater stiffness and hardness in the nanocomposites. Consequently, one-step PU is more prone to deformation in a TENG device compared to two-step PU.

On the other hand, in the plastic deformation zone, a contrasting effect is observed: higher CNC content results in reduce material extensibility. In this region of the stress-strain curve, the soft segment typically stretches due to the interconnection between hard and soft segments. However, the presence of CNC impedes or obstructs the chain extensibility. Both segments in PU contribute to strain-induced crystallization (SIC), which involves the rotation and alignment of hard segments and the stretching of soft segments (Khan et al., 2010). This SIC behavior significantly impacts the electrification performance and the induced intermolecular forces (Šutka et al., 2020, Xu et al., 2019) leading to changes in the effective contact area (Šutka et al., 2019, Lee et al., 2013). During stretching, applied stress can alter the conformation of functional groups exposed on the polymer surface (Wang et al., 2019, Wang et al., 2019, Sow et al., 2012). SIC can be a valuable feature for contact electrification and the development of TENGs. Figure 4 shows a soft plateau in the middle of the stress-strain curve for neat PU and also with 0.1 % wt CNC in both PU families. This suggests that neat PUs and those with lower CNC concentrations exhibit SIC behavior. Conversely, high CNC concentrations (0.5, 1 and 2 % wt CNC) disrupt stress-induced crystallization, making these materials less suitable for triboelectrification due to increased hardness and lower extensibility.

Table 3 shows the mechanical parameters obtained from the stress-strain curves shown in Figure 4. The two-step PU

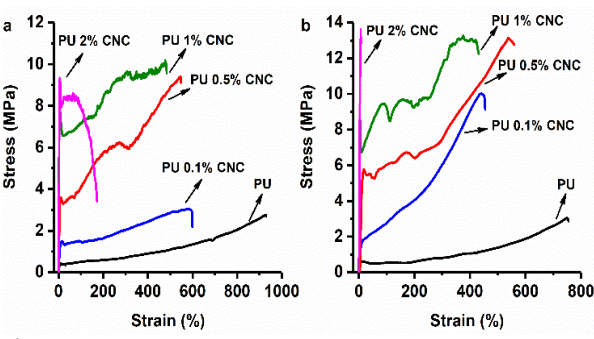


Fig 4. Strain-stress curves of a) one-step PU and b) two-step PU, and their nanocomposites.

family exhibited higher values for most mechanical parameters (Young's modulus, yield points, ultimate strength, strain at break, and toughness) compared to the one-step PU. This indicates that the two-step PU, both in its neat form and as a nanocomposite, has superior mechanical properties. Based on the data in Table 3, one-step PU is a softer, more flexible material that deforms more easily at low strains, which is advantageous during the triboelectrification process. Both PU families exhibit SIC behavior at very low CNC concentration (0.1 % wt), suggesting that low concentrations of CNC are below the percolation threshold and promote effective interaction and interconnection between the hard and soft segments of both PUs.

3.4 Physical properties of PU

3.4.1 Hardness

Equations 1 and 2, the Reuss model predicts Young's modulus with good accuracy for neat PU and nanocomposites with lower CNC concentrations (0.1 and 0.5 % wt). However, at higher CNC concentrations (1 and 2 % wt) hardness values decrease. This decrease can be attributed to the inhomogeneities in PU nanocomposites caused by percolation effects. Hardness

measurements create small holes on the surface, suggesting a disruption in the interconnection between the soft and hard segments of PU during the penetration process. The contact area is a crucial factor affecting the charge capacity of triboelectric nanogenerators. Therefore, it is essential to obtain the contact area between PU and external material (copper). Guan found a relationship between type A shore hardness and the contact area of soft materials in TENG experiments. Their results indicate that lower type A shore hardness values result in a larger contact area and consequently more generated charge. The recorded results show that transferred charge decreases nonlinearly with hardness, with the rate of decrease slowing as hardness increases. In other words, softer PU materials generate higher transferred charges with each contact (Guan et al., 2021).

3.4.2 Coefficient of friction (COF)

Given the inherent relationship between triboelectricity and friction, combining an electric energy collection system with friction can also facilitate the design of in-situ sensor for monitoring frictional states, which is important for practical applications (Erdemir et al., 2000). Liqiang Zhang reports that reducing the coefficient of friction (COF) to less than 0.01 is significant for triboelectric nanogenerators (TENGs), they found that a high friction coefficient detrimental to the development of TENGs (Zhang et al., 2022). The differences in friction coefficients can be related to the hardness values of the surface. A surface with greater hardness exhibits less drag resistance and lower apparent friction coefficients. CNC can migrate to the surface films, and with higher cellulose content, the material surfaces become harder, allowing for the formation of agglomerates that can be dispersed on the external surface (Hormaiztegui et al., 2020, Zakani et al., 2022 de Oliveira et al., 2013).

3.4.3 Surface energy

Table 4 lists the surface energy of both PU families obtained from equations 6-8. The surface tension of solids is differentiated into polar and dispersive interactions. The results show a slight difference in solid surface tension. Essentially, the two PU nanocomposites exhibit opposite behaviors in terms of surface energy. Nanocomposites from the one-step PU family show higher values for dispersive forces and lower values of the polar part of surface tension. In contrast, the two-step PU family shows the opposite behavior. Non-chain extended PU exhibits better compatibility with cooper electrodes, as its dispersive

part is closer in value compared to the two-step PU, also there is a minimal difference in the total surface tension between the two PU types, suggesting low adhesion between electrodes and the PUs. PU materials with low surface tension have certain advantages. For instance, Jang reports that in TENG applications, low surface energy materials lead to increased air trapping at the interface between copper and PU and reduced moisture absorption. According to the data in Table 4, the onestep PU family composites exhibit lower polar and higher dispersive force contributions on the surface compared to the two-step PU family materials, this suggests a difference in hydrophobicity. In this context, one-step PU can effectively prevent the formation of a moisture layer or minimize the contact area between the moisture layer and PU surface. This is because moisture has greater difficulty infiltrating surface with hydrophobic properties. Such phenomena can lead to a significant decrease in triboelectric charging capacity; therefore, hydrophobicity helps maintain stable performance in various environments (Jang et al., 2016). As observed earlier, the hydrogen bonding detected by FTIR in two-step PU is related to the polar part of chain extended PU. During triboelectric experiments, the output voltage performance can be modulated by modifying the PU surface with different functional groups. In this case, PU with a chain extender containing an amine group exhibits lower voltage output compared to one-step PU.

Until now, several successful water-TENGs have been reported (Cheng *et al.*, 2014, Liang *et al.*, 2015), most of which require micro-/nanostructures and hydrophobic surfaces to maximize performance. Hydrophobicity is a key factor in optimizing TENG performance. Since the metallic surface used in this work is intrinsically hydrophilic due to the presence of native oxide, a low surface energy coating is necessary for PU polymers. It is also important to consider the chemical composition of the PU surface, as it significantly affects surface wettability. Good wettability and easy detachment between PU and copper contribute to high-fidelity surface transfer from PU to copper. According to Jin, TENG devices that effectively repel moisture from the materials surface maximize TENG output (Jin *et al.*, 2018).

The triboelectric effect results from several parameters: charge affinity, interaction between triboelectric layers, mode of interaction (sliding or contact-separation), mechanical properties, surface geometry, and other variables discussed earlier. Charge affinity, determined by the chemical compositions of the materials, affects their ability to attract electrons. The chemical structures of the materials influence their polarities, which are crucial in triboelectrification

Table 4

Physical properties of one-step PII and two-step PI

Sample	Hardness	COF	COF	Surface energy	Surface energy	Surface Energy σ_s
	(shore A)	Static friction	Dynamic friction	σ_s^D mJ/m ²	$\sigma_s^P mJ/m^2$	mJ/m ²
		One	-step PU			
Neat PU	62.5 ± 4.6	0.56 ± 0.02	0.42 ± 0.01	16.30	19.98	36.29
PU 0.1 %	67.3 ± 6.0	0.49 ± 0.02	0.38 ± 0.02	15.83	20.37	36.21
PU 0.5 %	78 ± 3.7	0.43 ± 0.02	0.29 ± 0.01	13.77	28.63	42.40
PU 1 %	66.8 ± 3.3	0.44 ± 0.02	0.30 ± 0.01	12.05	22.04	34.09
PU 2 %	73.6 ± 5.6	0.38 ± 0.03	0.28 ± 0.02	11.29	29.13	40.42
		Two	-step PU			
Neat PU	77.5 ± 6.82	0.73 ± 0.06	0.41 ± 0.04	7.24	33.66	40.90
PU 0.1 %	80 ± 5.6	0.48 ± 0.04	0.35 ± 0.02	6.08	35.94	42.02
PU 0.5 %	94.2 ± 5.3	0.43 ± 0.02	0.29 ± 0.01	9.44	37.53	46.97
PU 1 %	88 ± 6.7	0.40 ± 0.02	0.30 ± 0.03	8.43	36.35	44.78
PU 2 %	82 ± 4.6	0.42 ± 0.03	0.30 ± 0.02	6.27	42.11	48.39
Cu	-	_	-	30.32	3.68	34.00

processes. The interaction between triboelectric layers is influenced by the surface energies of the materials and determines the energy difference at the interface, guiding electron transfer. The mode of interaction (sliding or contact-separation) affects the effective contact area of the interface (Kim *et al.*, 2017). When two surfaces come into full contact, for example, through a shaker, electrons transfer from the material with higher surface energy to the material with low surface energy (Wang *et al.*, 2016).

3.5 DFT Calculations

To study the potential distribution of functional groups in a segment of PU, chain elements were calculated using density functional theory (DFT). Figure 5 shows the repeating units of both PU families, including the HOMO and LUMO orbitals state (Frisch *et al.*, 2016, Li *et al.*, 2020), which contain electrons that can easily be donated during the triboelectric process. The observed differences in results are proposed to be due to the significant electronegativity difference between the amine group (from the chain extender) and the hydroxyl group, rather than any other combination (Li *et al.*, 2020).

Many studies have revealed that the characteristics and density of functional groups in a polymer can influence the electron transfer process during contact electrification (Tao et al., 2021, Wang et al., 2021, Lapčinskis et al., 2021, Xu et al., 2019, Sow et al., 2012). For commonly used stretchable triboelectric materials, such as PUs, the strain applied during triboelectrification can induce significant changes in the electrification process. Typically, changes in the effective contact area (Šutka et al., 2020, Lee et al., 2013) and the induced intermolecular forces (Šutka et al., 2019, Liu et al., 2022) are considered primary factors affecting electrification performance. During stretching, the applied stress may alter the composition of functional groups exposed on the polymer surface. Additionally, stretching-induced crystallization of soft segments may occur in these PUs and nanocomposites (Wang et al., 2019, Kwak et al., 2019). The electrostatic potential diagram of a segmented chain of both PU is shown in 5, where the blue and red areas represent positive and negative potential regions, corresponding to electron-poor and electron-rich areas, respectively. Therefore, the C-C bonds provide an electron donating conjugation effect within PU molecule. Molecular orbital simulation diagrams also show that the electron cloud density associated with the C-O bond is greater than that associated with the C-H bond. Consequently, the crystallization of the soft segment in PU arranges the molecular chains more orderly, exposing the electron-poor areas (C-H) at the surface while hiding the electron-donating bonds (C-O) in the bulk region. This arrangement enhances the overall electron-withdrawing capability of PU. Meanwhile, the SIC effect also alters the functional groups in PU, significantly reducing the presence of ethyl (-CH₂CH₃), methylene (-CH₂), urethane and urea bonds due to hydrogen bonding interactions. The reduction of electron-donor groups in the surface region leads to a strain-induced shift in the triboelectric series. FTIR has been used to verify changes in the surface functional groups of PU. Specifically, a decrease in the ether group in two-step PU nanocomposites and an increase in the C-O group in one-step PU nanocomposites near the surface region have been confirmed (Lorenzini et al., 2013). Figure 5 (inset) shows the partial spectra of one-step and two-step PU in the stretching C-O region. Both spectra were normalized to 1 based on the highest signal (carbonyl peak) to facilitate the visualization and comparison of ether bond intensities. In the case of one-step PU, the intensity of the nanocomposite bands is greater than that of

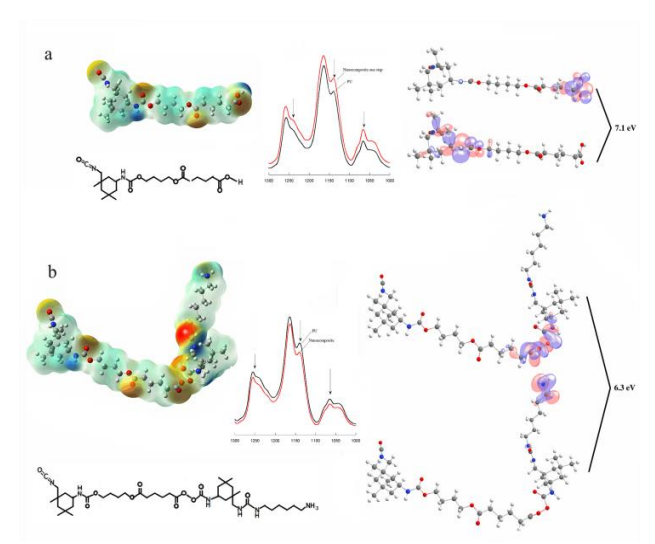


Fig 5. Electrostatic potential maps and electron cloud orbitals corresponding to the HOMO and LUMO of a) one-step PU and b) two-step PU, calculated at the B3LYP/cc-pVTZ level.

neat PU, whereas, for two-step PU, the intensity of the nanocomposites bands is lower compared to neat PU. This suggests that C-O bonds are more available during the triboelectrification process.

The highest occupied molecular orbital (HOMO) is a state filled with electrons, making it readily capable of donating electrons to a material in contact through friction during the triboelectric process. Thus, the hydrogen atoms in a molecule or functional group can give rise to HOMO states. Complementarily, the distributions of the lowest unoccupied molecular orbital (LUMO) for the PU families, which can act as electron acceptor states, were also calculated in this simulation. When triboelectrification occurs between PU and copper, charge can be transferred from the HOMO of PU, making it positively charged, to the LUMO of the copper terminal, making it negatively charged. According to this assertion, electrons transfer from the hard segment to the soft segment. This occurs because the hydrogen atoms in the diisocyanate can contribute with more electrons to the surface of the counter material during repeated contact, leaving the surface positively charged (Ning et al., 2017; Jin et al., 2020; Mattia et al., 2007; Kim et al., 2023; Guo et al., 2023). The interactions between hydrogen atoms (likely due to van der Waals forces, the large surface area, and the polarizability around the diisocyanates hydrogen atoms) can result in a more robust and complex polymeric structure (Lorenzini et al., 2013). In Figure 5, the separation between the HOMO and LUMO is observed. A larger HOMO-LUMO orbital energy gap indicates greater resistance to changes in electronic distribution and polarization. This suggests that one-step PU, with its higher band gap values, behaves more like a dielectric material and can store more charge compared to two-step PU. According to Lorenzini, urethane bonds have a higher dielectric constant than urea bonds due to their electronegativity. Additionally, it is reported that increasing the number of carbons in the backbone lowers the dielectric constant, which is attributed to the increased free volume that reduces the number of polarizable groups per unit volume (Simpson et al., 1997; Hwang et al., 2006; Chen et al., 2016). In this sense, two-step PU contains both characteristics (urea bonds and a higher number of carbons due to the chain extender) and thus has a lower capacity to generate triboelectric gain compared to one-step PU.

Table 5Measuring the electrical performance of TENG and calculating capacitance and permittivity

Sample	Permittivity	Capacitance (pF)	Voltage (V)	Current (µA)	Power (µW)
		One-ste	ep PU		
Neat PU	2.19	25.00	1.47 ± 0.05	0.35 ± 0.01	0.51 ± 0.07
PU 0.1 %	2.47	29.20	2.04 ± 0.09	0.43 ± 0.02	0.89 ± 0.09
PU 0.5 %	2.20	25.92	1.25 ± 0.05	0.30 ± 0.01	0.39 ± 0.05
PU 1 %	2.19	25.90	1.32 ± 0.06	0.29 ± 0.01	0.38 ± 0.08
PU 2 %	2.16	26.43	1.15 ± 0.04	0.19 ± 0.05	0.22 ± 0.05
		Two-ste	ep PU		
Neat PU	2.18	24.90	0.98 ± 0.02	0.31 ± 0.01	0.31 ± 0.05
PU 0.1 %	2.62	29.00	1.49 ± 0.06	0.35 ± 0.01	0.46 ± 0.07
PU 0.5 %	2.45	28.90	1.08 ± 0.02	0.27 ± 0.01	0.29 ± 0.03
PU 1 %	2.18	27.60	0.60 ± 0.02	0.17 ± 0.01	0.10 ± 0.05
PU 2 %	2.27	27.70	0.75 ± 0.02	0.19 ± 0.01	0.14 ± 0.04

3.6 Measurements TENG

The measurements of capacitance and dielectric constant are summarized in Table 5. It is observed that maximum values are archived with a concentration of 0.1 % wt of CNC, followed by a slight tendency to decrease in both families of PU. In this context, a low concentration of CNC implies enhanced dispersion of the nanofiller, leading to better distribution within both PU segments. As mentioned earlier in the FTIR characterization, these parameters may be related to hydrogen bonding content. Table 5 shows the calculations obtained using equation 9, where a direct relationship between dielectric constant and capacitance is observed. Higher values of capacitance or permittivity indicate a greater capacity for the electrification process. It was previously note that the dielectric constant is a key parameter influencing TENG systems. A high dielectric material is more susceptible to interacting with electric fields and more likely to polarize. Therefore, calculating the dielectric constant is crucial, as it serves as an indicator of the proper functioning of TENG systems and is a key to their effectiveness (Hwang et al., 2006; Chen et al., 2026). In this context, one-step PU, with a dielectric constant of 2.19, is a promising candidate for use in these types of devices.

The lower gain in voltage and current in nanocomposites with high CNC content is due to the weak polarization tendency of cellulose/nanocellulose, which restricts its capacity to generate surface charge (Xia et al., 2017, Adonijah et al., 2020, Sriphan et al 2020, Wang et al., 2017), this makes it a weak

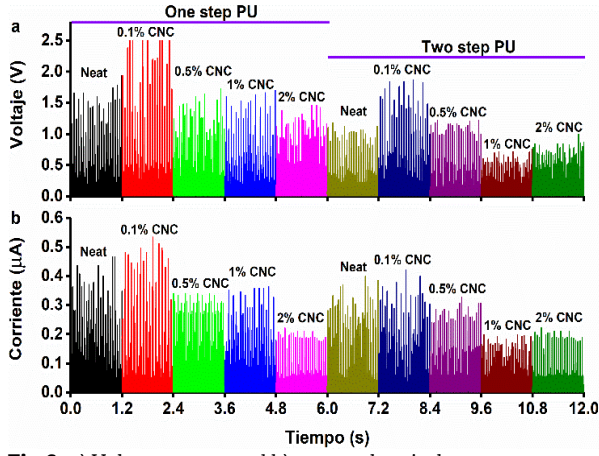


Fig 6. a) Voltage curves and b) output electrical current curves versus time for the different TENG systems in both PU families with varying CNC concentrations.

tribopositive material resulting in inferior output performance of nanocellulose-based TENGs (Yao *et al.*, 2017).

Also, the increased output power of the one-step PU TENG may be attributed to its sufficiently rough surface, which has a friction coefficient of 0.56 (see Table 4). When in contact with the copper foil, the friction between the surfaces generates a triboelectric charge density on the PU surface. Additionally, the PU exhibits elasticity, which, when subjected to external force, increases the surface contact area between the PU and the copper foil. This deformation helps cover gaps between the surfaces, enhancing contact friction and thereby increasing the triboelectric charge density, resulting in improved TENG performance (Mi et al., 2018; Mao et al., 2015; Tcho et al., 2017). The elasticity of the PU is confirmed by its measured rigidity, with a hardness value of 62.5, indicating good flexibility when compressed. This is also related to Young's modulus, which is relatively low at 6.73 Mpa, suggesting good longitudinal elasticity. Furthermore, FTIR characterization (Figure 2a) and DPS calculation (see Table 1) reveal that the one-step PU film contains a higher proportion of soft segments. These soft segments interact to enhance the ordering of the polymer chains, thereby improving thermal, viscoelastic and superficial properties (Guan et al., 2021). On the other hand, the similar surface energy of both the copper foils and the one-step PU films indicates effective interaction and better adhesion between these two surfaces.

The two-step PU has dielectric constant and capacitance values that are closer to those of the one-step PU. However, it exhibits greater rigidity and a higher coefficient of friction, which impedes deformation and results in a reduced contact area and lower charge density, leading to poorer TENG performance. The increased rigidity of nanocomposites with high CNC content is reflected in a higher Young's modulus, which is more pronounced in two-step nanocomposites, where the Young's modulus is 2.5 times higher than that of the one-step PU. Furthermore, the permeation limit is reached, causing CNC agglomeration that adversely affects the surface contact area and disrupts the electrical charge capture process (Jin *et al.*, 2020; Chen *et al.*, 2016).

Figure 6a shows the open-circuit voltage curves, while Figure 6b shows the rectified output electric short-circuit current curves as a function of time for the different TENG systems studied, under operating conditions of 23 Hz and a force of approximately 4 N. The black and olive green curves, representing the neat PU samples for the one-step and two-step PU systems respectively (i.e., the reference systems without CNC), show voltages of 1.47 V and 0.98 V and currents of 0.35 μA and 0.31 μA , respectively. This corresponds to a difference of approximately 64.5 % in output power between these two systems (see Table 5). Figure 6 also shows the voltage and

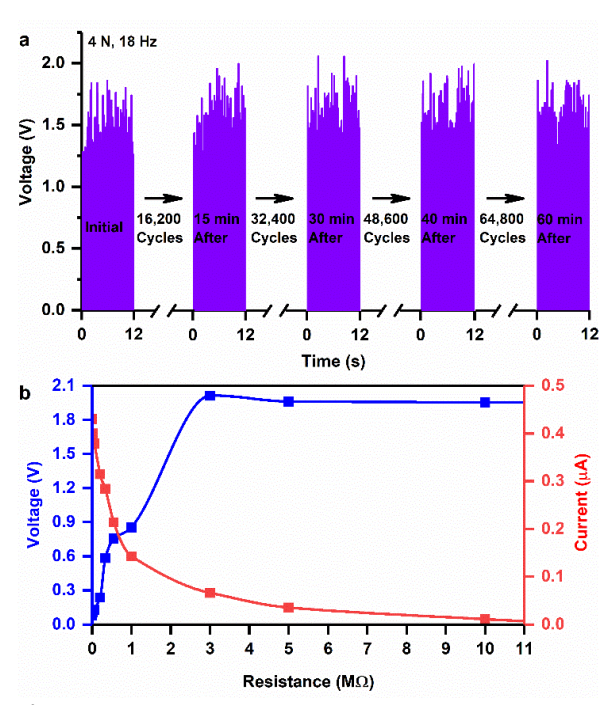


Fig 7. a) Durability and stability of the output voltage of the one-step PU TENG system with 0.1 % CNC, and b) Electrical output of the one-step PU TENG system with 0.1 % CNC at different external resistances.

current outputs of all PU samples prepared; it is evident that the curves for the one-step PU exhibit higher values compared to the two-step PU. A slight trend can be observed in the nanocomposites, where the values decrease as the CNC concentration increase, with the maximum values observed at 0.1 % wt CNC for both PU families. The red curve corresponds to a one-step PU sample with 0.1 % wt CNC, which exhibits the highest values: a voltage of 2.04 V, an electrical current of 0.34 μA , and an output power of 0.89 μW . This represents a 74.5 % increase in power compared to the neat one-step PU. A similar behavior is observed in the two-step PU, where 0.1 % wt CNC also yields the highest values within this PU family.

To evaluate which of the two PU families has more potential market applications, the output electrical signals of both PU families filled with $0.1\,\%$ wt CNC, which showed the best



Fig 8. Photograph of the LEDs being turned on by the one-step PU TENG system with 0.1 % wt CNC.

performance, were compared. The mechanical properties with CNC incorporation were also considered. Although the rigidity of the two-step PU nanocomposites (e.g., Young's modulus, hardness and friction coefficient) is higher, resulting in slightly lower surface charge density, this increased rigidity may help maintain shape, reduce mechanical wear, and provide a longer useful lifetime compared to the one-step PU.

On the other hand, the stability and durability of the TENG system using one-step PU with 0.1 % wt CNC were tested by subjecting the system to mechanical movement for 60 minutes with a compression force of approximately 4 N and a frequency of 32 Hz. During this process, the output voltage was measured every 16200 cycles over a period of 15 minutes (see Figure 7a). The sample exhibited only slight variations between 16200 to 64800 cycles. This study indicates that the TENG system maintains stable electric charge production over extended periods of continuous operation, demonstrating good stability and durability of nanocomposite films. This stability may be attributed to the previously calculated mechanical properties, such as elastic modulus, which help resist localized deformation and stress. These properties contribute to maintaining the shape of the samples under mechanical compression for prolonged periods. Additionally, this study suggests that the materials tested are suitable as dielectric materials, offering versatility and reliability in TENG systems.

Figure 7b shows the output voltage and electric current measurements of the one-step PU TENG system filled with 0.1 % wt CNC at different external resistances. The voltage decreases with lower resistance and increases with high resistance, reaching a maximum of 2.01 V with 3 M Ω and then remaining relatively unchanged. In contrast, the current shows the opposite trend, peaking at 0.011 μ A with a 10 M Ω resistance. These measurements reveal two intersecting curves, indicating the optimal (ideal) operating conditions of the TENG device. The maximum power output of the TENG can be adjusted by varying the external resistance, which is crucial for its application in a wide range of uses. Additionally, Figure 8 shows a photograph of the system with rectified current successfully powering 35 commercial red LEDs connected in a parallel configuration with a 1 µF capacitor. The LEDs turn on every 5 seconds, demonstrating the system's functionality. The test setup included a one-step PU TENG system with 0.1 % wt CNC, which effectively generated a sufficient electric current to power the LEDs. The LEDs, arranged in parallel, provided consistent illumination, and the 1 μF capacitor helped stabilize the power output, ensuring that the system could deliver energy in a controlled manner. This test demonstrates that the PU TENG system is functional and capable of generating a useful electric current for self-powered devices with low energy consumption.

6. Conclusion

A TENG device was built using two families of PU and their nanocomposites filled with CNC to relate physical and chemical properties to the electrical output of the TENG devices. The findings describe the main properties involved in the triboelectrification process. Specifically, the contribution of hydrogen bonding may be a factor in choosing a PU with a simple structure (non-chain extended) over a two-step PU. This is because the increase in hard segments in the two-step PU generates more urea bonds, leading to increased hydrogen bonding and more polar interactions, which hinder polarization in the PU. One of the most important properties to consider in triboelectrification in a PU matrix is stress-induced crystallization (SIC), which affects the mechanical behavior of

PU by allowing it to exhibit extensibility over a wide range of deformations. According to this work, it is recommended to use chain extenders with diols instead of diamines and to select diisocyanates with a high hydrogen atom content, such as cycloaliphatic or aromatic isocyanates. Using a lower content of nanofiller, bellow the percolation threshold, is advisable due to the transfer of stiffness from the nanoparticles to the matrix. Incorporating crystallizable diols as soft segment enhances electrostatic interactions in well-packed structures. While crystalline nanocellulose may provide only minimal advantages for charge acquisition, it can significantly improve the structural ordering of hard and soft segment in PU.

Author Contributions: Jose M. Blancas-Flores and Gilberto Rocha-Ortiz: Conceptualization, methodology, formal analysis, writing—original draft, Víctor H. Antolín-Cerón; supervision, resources, project administration, Juan Morales-Rivera, H.A. Andrade-Melecio,; writing—review and editing, project administration, validation, Pablo D. Astudillo-Sanchez; writing—review and editing, project administration, validation. Irán F. Hernandez Ahuactzi: Data curation and simulation software, José J. Cabrera-Chavarria: Funding acquisition All authors have read and agreed to the published version of the manuscript.

Funding: The author(s) received no financial support for the research, authorship, and/or publication of this article.

Conflicts of Interest: The authors declare no conflict of interest.

References

- Adonijah Graham, S., Dudem, B., Patnam, H., Mule, A. R., & Yu, J. S. (2020). Integrated design of highly porous cellulose-loaded polymer-based triboelectric films toward flexible, humidity-resistant, and sustainable mechanical energy harvesters. *ACS Energy Letters*, 5(7), 2140-2148. https://doi.org/10.1021/acsenergylett.0c00635
- Antolín-Cerón, V. H., González-López, F. J., Astudillo-Sánchez, P. D., Barrera-Rivera, K. A., & Martínez-Richa, A. (2022). Highperformance polyurethane nanocomposite membranes containing cellulose nanocrystals for protein separation. *Polymers*, 14(4), 831. https://doi.org/10.3390/polym14040831
- Arrieta, M. P., López, J., López, D., Kenny, J. M., & Peponi, L. (2016). Biodegradable electrospun bionanocomposite fibers based on plasticized PLA-PHB blends reinforced with cellulose nanocrystals. *Industrial Crops and Products*, 93, 290-301. https://doi.org/10.1016/j.indcrop.2015.12.058
- Bakošová, D., & Bakošová, A. (2022). Testing of rubber composites reinforced with carbon nanotubes. *Polymers*, *14*(15), 3039. https://doi.org/10.3390/polym14153039
- Bunriw, W., Harnchana, V., Chanthad, C., & Huynh, V. N. (2021). Natural rubber-TiO2 nanocomposite film for triboelectric nanogenerator application. *Polymers*, 13(13), 2213. DOI: 10.1039/c8nr05872e
- Chen, J., Guo, H., He, X., Liu, G., Xi, Y., Shi, H., & Hu, C. (2016). Enhancing performance of triboelectric nanogenerator by filling high dielectric nanoparticles into sponge PDMS film. *ACS applied materials* & interfaces, 8(1), 736-744. https://doi.org/10.1021/acsami.5b09907
- Chen, S. Y., Zhuang, R. Q., Chuang, F. S., & Rwei, S. P. (2021). Synthetic scheme to increase the abrasion resistance of waterborne polyurethane—urea by controlling micro-phase separation. *Journal of Applied Polymer Science*, 138(24), 50561. https://doi.org/10.1002/app.50561
- Cheng, B. X., Gao, W. C., Ren, X. M., Ouyang, X. Y., Zhao, Y., Zhao, H., ... & Li, R. K. (2022). A review of microphase separation of polyurethane: Characterization and applications. *Polymer Testing*, 107,107489.https://doi.org/10.1016/j.polymertesting.202 2.107489
- Cheng, G., Lin, Z. H., Du, Z. L., & Wang, Z. L. (2014). Simultaneously harvesting electrostatic and mechanical energies from flowing

- water by a hybridized triboelectric nanogenerator. ACS nano, θ(2), 1932-1939. https://doi.org/10.1021/nn406565k
- Cranston, E. D., & Gray, D. G. (2006). Morphological and optical characterization of polyelectrolyte multilayers incorporating nanocrystalline cellulose. *Biomacromolecules*, 7(9), 2522-2530. https://doi.org/10.1021/bm0602886
- de Oliveira Patricio, P. S., Pereira, I. M., da Silva, N. C. F., Ayres, E., Pereira, F. V., & Oréfice, R. L. (2013). Tailoring the morphology and properties of waterborne polyurethanes by the procedure of cellulose nanocrystal incorporation. *European Polymer Journal*, 49(12), 3761-3769. https://doi.org/10.1016/j.eurpolymi.2013.08.006
- Erdemir, A., Eryilmaz, O. L., & Fenske, G. (2000). Synthesis of diamondlike carbon films with superlow friction and wear properties. *Journal of Vacuum Science & Technology A: Vacuum, Surfaces, and Films, 18*(4), 1987-1992. https://doi.org/10.1116/1.582459
- Fan, F. R., Tian, Z. Q., & Wang, Z. L. (2012). Flexible triboelectric generator. *Nano* energy, 1(2), 328-334. https://doi.org/10.1016/j.nanoen.2012.01.004
- Fortunati, E., Armentano, I., Zhou, Q., Iannoni, A., Saino, E., Visai, L., ... & Kenny, J. M. (2012). Multifunctional bionanocomposite films of poly (lactic acid), cellulose nanocrystals and silver nanoparticles. *Carbohydrate polymers*, 87(2), 1596-1605. https://doi.org/10.1016/j.carbpol.2011.09.066
- Frisch, M., & Clemente, F. MJ Frisch, GW Trucks, HB Schlegel, GE Scuseria, MA Robb, JR Cheeseman, G. Scalmani, V. Barone, B. Mennucci, GA Petersson, H. Nakatsuji, M. Caricato, X. Li, HP Hratchian, AF Izmaylov, J. Bloino and G. Zhe, Gaussian, 9.
- Gent, A. N. (1958). On the relation between indentation hardness and Young's modulus. *Rubber Chemistry and Technology*, *31*(4), 896-906. https://doi.org/10.5254/1.3542351
- Guan, D., Cong, X., Li, J., Shen, H., Zhang, C., & Gong, J. (2021). Quantitative characterization of the energy harvesting performance of soft-contact sphere triboelectric nanogenerator. *Nano Energy*, 87, 106186. https://doi.org/10.1016/j.nanoen.2021.106186
- Guan, D., Cong, X., Li, J., Shen, H., Zhang, C., & Gong, J. (2021).
 Quantitative characterization of the energy harvesting performance of soft-contact sphere triboelectric nanogenerator. *Nano Energy*, 87, 106186. https://doi.org/10.1016/j.nanoen.2021.106186
- Guo, Z. H., Zhang, Z., An, K., He, T., Sun, Z., Pu, X., & Lee, C. (2023). A wearable multidimensional motion sensor for AI-enhanced VR sports. Research, 6, 0154. DOI: 10.34133/research.0154
- Hormaiztegui, M. E. V., Daga, B., Aranguren, M. I., & Mucci, V. (2020). Bio-based waterborne polyurethanes reinforced with cellulose nanocrystals as coating films. *Progress in Organic Coatings*, 144, 105649. https://doi.org/10.1016/j.porgcoat.2020.105649
- Hwang, H. J., Li, C. H., & Wang, C. S. (2006). Dielectric and thermal properties of dicyclopentadiene containing bismaleimide and cyanate ester. Part IV. *Polymer*, 47(4), 1291-1299. https://doi.org/10.1016/j.polymer.2005.12.040
- Jang, D., Kim, Y., Kim, T. Y., Koh, K., Jeong, U., & Cho, J. (2016). Force-assembled triboelectric nanogenerator with high-humidity-resistant electricity generation using hierarchical surface morphology. *Nano Energy*, 20, 283-293. https://doi.org/10.1016/j.nanoen.2015.12.021
- Jin, L., Xiao, X., Deng, W., Nashalian, A., He, D., Raveendran, V., ... & Chen, J. (2020). Manipulating relative permittivity for high-performance wearable triboelectric nanogenerators. *Nano Letters*, 20(9), 6404-6411. https://doi.org/10.1021/acs.nanolett.0c01987
- Jin, S., Wang, Y., Motlag, M., Gao, S., Xu, J., Nian, Q., ... & Cheng, G. J. (2018). Large-area direct laser-shock imprinting of a 3D biomimic hierarchical metal surface for triboelectric nanogenerators. *Advanced materials*, 30(11), 1705840. https://doi.org/10.1002/adma.201705840
- Khan, U., Blighe, F. M., & Coleman, J. N. (2010). Selective mechanical reinforcement of thermoplastic polyurethane by targeted insertion of functionalized SWCNTs. *The Journal of Physical Chemistry* C, 114(26), 11401-11408. https://doi.org/10.1021/jp102938q
- Kim, H. J., Yim, E. C., Kim, J. H., Kim, S. J., Park, J. Y., & Oh, I. K. (2017). Bacterial nano-cellulose triboelectric nanogenerator. *Nano Energy*, 33, https://doi.org/10.1016/j.nanoen.2017.01.035

- Kim, J. K., Han, G. H., Kim, S. W., Kim, H. J., Purbia, R., Lee, D. M., ... & Baik, J. M. (2023). Electric-field-driven interfacial trapping of drifting triboelectric charges via contact electrification. *Energy & Environmental Science*, 16(2), 598-609. https://doi.org/10.1039/D2EE03114K
- Kwak, S. S., Kim, S. M., Ryu, H., Kim, J., Khan, U., Yoon, H. J., ... & Kim, S. W. (2019). Butylated melamine formaldehyde as a durable and highly positive friction layer for stable, high output triboelectric nanogenerators. *Energy & Environmental Science*, 12(10), 3156-3163. https://doi.org/10.1039/C9EE01267B
- Lapčinskis, L., Linarts, A., Mālnieks, K., Kim, H., Rubenis, K., Pudzs, K., ... & Šutka, A. (2021). Triboelectrification of nanocomposites using identical polymer matrixes with different concentrations of nanoparticle fillers. *Journal of Materials Chemistry A*, 9(14), 8984-8990. https://doi.org/10.1039/D0TA12441A
- Lee, J. H., Hinchet, R., Kim, S. K., Kim, S., & Kim, S. W. (2015). Shape memory polymer-based self-healing triboelectric nanogenerator. *Energy & Environmental Science*, 8(12), 3605-3613. https://doi.org/10.1039/C5EE02711J
- Lee, S., Lee, Y., Kim, D., Yang, Y., Lin, L., Lin, Z. H., ... & Wang, Z. L. (2013). Triboelectric nanogenerator for harvesting pendulum oscillation energy. *Nano Energy*, *2*(6), 1113-1120. https://doi.org/10.1016/j.nanoen.2013.08.007
- Li, S., Fan, Y., Chen, H., Nie, J., Liang, Y., Tao, X., ... & Wang, Z. L. (2020). Manipulating the triboelectric surface charge density of polymers by low-energy helium ion irradiation/implantation. *Energy & Environmental Science*, *13*(3), 896-907. https://doi.org/10.1039/C9EE03307F
- Li, S., Nie, J., Shi, Y., Tao, X., Wang, F., Tian, J., ... & Wang, Z. L. (2020). Contributions of different functional groups to contact electrification of polymers. *Advanced Materials*, *32*(25), 2001307. https://doi.org/10.1002/adma.202001307
- Liang, Q., Yan, X., Gu, Y., Zhang, K., Liang, M., Lu, S., ... & Zhang, Y. (2015). Highly transparent triboelectric nanogenerator for harvesting water-related energy reinforced by antireflection coating. *Scientific* reports, 5(1), 9080. https://doi.org/10.1038/srep09080
- Liu, Z., Li, S., Lin, S., Shi, Y., Yang, P., Chen, X., & Wang, Z. L. (2022).

 Crystallization-induced shift in a triboelectric series and even polarity reversal for elastic triboelectric materials. *Nano letters*, 22(10),

 https://doi.org/10.1021/acs.nanolett.2c00767
- Lorenzini, R. G., Kline, W. M., Wang, C. C., Ramprasad, R., & Sotzing, G. A. (2013). The rational design of polyurea & polyurethane dielectric materials. *Polymer*, *54*(14), 3529-3533. https://doi.org/10.1016/j.polymer.2013.05.003
- Mao, Y., Geng, D., Liang, E., & Wang, X. (2015). Single-electrode triboelectric nanogenerator for scavenging friction energy from rolling tires. *Nano Energy*, 15, 227-234. https://doi.org/10.1016/j.nanoen.2015.04.026
- Marcos-Fernandez, A., Lozano, A. E., Gonzalez, L., & Rodriguez, A. (1997). Hydrogen Bonding in Copoly (ether— urea) s and Its Relationship with the Physical Properties. *Macromolecules*, 30(12), 3584-3592. https://doi.org/10.1021/ma9619039
- Margaronis, K., Busolo, T., Nair, M., Chalklen, T., & Kar-Narayan, S. (2021). Tailoring the triboelectric output of poly-L-lactic acid nanotubes through control of polymer crystallinity. *Journal of Physics: Materials*, 4(3), 034010. 10.1088/2515-7639/abf7de
- Mattia, J., & Painter, P. (2007). A Comparison of Hydrogen Bonding and Order in a Polyurethane and Poly (urethane— urea) and Their Blends with Poly (ethylene glycol). *Macromolecules*, 40(5), 1546-1554. https://doi.org/10.1021/ma0626362
- Mi, H. Y., Jing, X., Cai, Z., Liu, Y., Turng, L. S., & Gong, S. (2018). Highly porous composite aerogel based triboelectric nanogenerators for high performance energy generation and versatile self-powered sensing. *Nanoscale*, 10(48), 23131-23140. https://doi.org/10.1039/C8NR05872E
- Mi, H. Y., Jing, X., Zheng, Q., Fang, L., Huang, H. X., Turng, L. S., & Gong, S. (2018). High-performance flexible triboelectric nanogenerator based on porous aerogels and electrospun nanofibers for energy harvesting and sensitive self-powered sensing. *Nano*Energy, 48, 327-336.https://doi.org/10.1016/j.nanoen.2018.03.050

- Navarro-Baena, I., Kenny, J. M., & Peponi, L. (2014). Thermally-activated shape memory behaviour of bionanocomposites reinforced with cellulose nanocrystals. *Cellulose*, *21*, 4231-4246. https://doi.org/10.1007/s10570-014-0446-5
- Ning, N., Li, S., Sun, H., Wang, Y., Liu, S., Yao, Y., ... & Tian, M. (2017). Largely improved electromechanical properties of thermoplastic polyurethane dielectric elastomers by the synergistic effect of polyethylene glycol and partially reduced graphene oxide. *Composites Science and Technology*, 142, 311-320. https://doi.org/10.1016/j.compscitech.2017.02.015
- Niu, H., Du, X., Zhao, S., Yuan, Z., Zhang, X., Cao, R., ... & Li, C. (2018). Polymer nanocomposite-enabled high-performance triboelectric nanogenerator with self-healing capability. *RSC advances*, 8(54), 30661-30668. 10.1039/C8RA05305G
- Ourique, P. A., Ornaghi, F. G., Ornaghi, H. L., Wanke, C. H., & Bianchi, O. (2019). Thermo-oxidative degradation kinetics of renewable hybrid polyurethane–urea obtained from air-oxidized soybean oil. *Journal of Thermal Analysis and Calorimetry*, *137*, 1969-1979. https://doi.org/10.1007/s10973-019-08089-9
- Owens, D. K., & Wendt, R. C. (1969). Estimation of the surface free energy of polymers. *Journal of applied polymer science*, 13(8), 1741-1747. https://doi.org/10.1002/app.1969.070130815
- Pimentel G.C: and Mc-Clellan A.L., The hydrogen bond, W:H. Freeman, San Francisco 1960
- Saralegi, A., Rueda, L., Martin, L., Arbelaiz, A., Eceiza, A., & Corcuera, M. A. (2013). From elastomeric to rigid polyurethane/cellulose nanocrystal bionanocomposites. *Composites science and technology*, 88, 39-47. https://doi.org/10.1016/j.compscitech.2013.08.025
- Shen, J., Li, Z., Yu, J., & Ding, B. (2017). Humidity-resisting triboelectric nanogenerator for high performance biomechanical energy harvesting. *Nano Energy*, 40, 282-288. https://doi.org/10.1016/j.nanoen.2017.08.035
- Simpson, J. O., & Clair, A. S. (1997). Fundamental insight on developing low dielectric constant polyimides. *Thin Solid Films, 308,* 480-485. https://doi.org/10.1016/S0040-6090(97)00481-1
- Smith, M., Chalklen, T., Lindackers, C., Calahorra, Y., Howe, C., Tamboli, A., ... & Kar-Narayan, S. (2020). Poly-L-lactic acid nanotubes as soft piezoelectric interfaces for biology: Controlling cell attachment via polymer crystallinity. *ACS applied bio materials*, 3(4), 2140-2149. https://doi.org/10.1021/acsabm.0c00012
- Sow, M., Lacks, D. J., & Mohan Sankaran, R. (2012). Dependence of contact electrification on the magnitude of strain in polymeric materials. *Journal of Applied Physics*, 112(8). https://doi.org/10.1063/1.4761967
- Sow, M., Lacks, D. J., & Mohan Sankaran, R. (2012). Dependence of contact electrification on the magnitude of strain in polymeric materials. *Journal of Applied Physics*, 112(8). https://doi.org/10.1063/1.4761967
- Sriphan, S., Charoonsuk, T., Maluangnont, T., Pakawanit, P., Rojviriya, C., & Vittayakorn, N.. Advanced Materials Technologies, 2020, 5(5), 2000001. https://doi.org/10.1002/admt.202000001
- Sun, J., Pu, X., Liu, M., Yu, A., Du, C., Zhai, J., ... & Wang, Z. L. (2018). Self-healable, stretchable, transparent triboelectric nanogenerators as soft power sources. *ACS nano*, *12*(6), 6147-6155. https://doi.org/10.1021/acsnano.8b02479
- Sung, C. P., & Schneider, N. S. (1977). Temperature dependence of hydrogen bonding in toluene diisocyanate based polyurethanes. *Macromolecules*, 10(2), 452-458.
- Šutka, A., Mālnieks, K., Lapčinskis, L., Kaufelde, P., Linarts, A., Bērziņa, A., ... & Knite, M. (2019). The role of intermolecular forces in contact electrification on polymer surfaces and triboelectric nanogenerators. *Energy & Environmental Science*, *12*(8), 2417-2421. https://doi.org/10.1039/C9EE01078E
- Šutka, A., Mālnieks, K., Lapčinskis, L., Timusk, M., Kalniņš, K., Kovaļovs, A., ... & Grunlan, J. (2020). Contact electrification between identical polymers as the basis for triboelectric/flexoelectric materials. *Physical Chemistry Chemical Physics*, 22(23), 13299-13305. https://doi.org/10.1039/D0CP01947J
- Tao, X., Nie, J., Li, S., Shi, Y., Lin, S., Chen, X., & Wang, Z. L. (2021). Effect of photo-excitation on contact electrification at liquid-solid

- interface. ACS nano, 15(6), 10609-10617. https://doi.org/10.1021/acsnano.1c03358
- Tcho, İ. W., Kim, W. G., Jeon, S. B., Park, S. J., Lee, B. J., Bae, H. K., ... & Choi, Y. K. (2017). Surface structural analysis of a friction layer for a triboelectric nanogenerator. *Nano Energy*, 42, 34-42. https://doi.org/10.1016/j.nanoen.2017.10.037
- Vatankhah, E., Tadayon, M., & Ramakrishna, S. (2021). Boosted output performance of nanocellulose-based triboelectric nanogenerators via device engineering and surface functionalization. *Carbohydrate Polymers*, 266, 118120.
 - https://doi.org/10.1016/j.carbpol.2021.118120
- Wang, F., Yang, P., Tao, X., Shi, Y., Li, S., Liu, Z., ... & Wang, Z. L. (2021). Study of contact electrification at liquid-gas interface. *ACS nano*, 15(11), 18206-18213. https://doi.org/10.1021/acsnano.1c07158
- Wang, H. L., Guo, Z. H., Zhu, G., Pu, X., & Wang, Z. L. (2021). Boosting the power and lowering the impedance of triboelectric nanogenerators through manipulating the permittivity for wearable energy harvesting. ACS nano, 15(4), 7513-7521. https://doi.org/10.1021/acsnano.1c00914
- Wang, R., Fang, S., Xiao, Y., Gao, E., Jiang, N., Li, Y., ... & Baughman, R. H. (2019). Torsional refrigeration by twisted, coiled, and supercoiled fibers. *Science*, 366(6462), 216-221. DOI: 10.1126/science.aax6182
- Wang, S., Zi, Y., Zhou, Y. S., Li, S., Fan, F., Lin, L., & Wang, Z. L. (2016). Molecular surface functionalization to enhance the power output of triboelectric nanogenerators. *Journal of Materials Chemistry A*, 4(10), 3728-3734. https://doi.org/10.1039/C5TA10239A
- Wang, X., Yao, C., Wang, F., & Li, Z. (2017). Cellulose-based nanomaterials for energy applications. *Small*, *13*(42), 1702240. https://doi.org/10.1002/smll.201702240
- Wang, Y., Yang, Y., & Wang, Z. L. (2017). Triboelectric nanogenerators as flexible power sources. npj Flexible Electronics, 1(1), 10. https://doi.org/10.1038/s41528-017-0007-8
- Wang, Z., Sun, B., Lu, X., Wang, C., & Su, Z. (2019). Molecular orientation in individual electrospun nanofibers studied by polarized AFM–IR. *Macromolecules*, 52(24), 9639-9645. https://doi.org/10.1021/acs.macromol.9b01778
- Xia, X., Chen, J., Guo, H., Liu, G., Wei, D., Xi, Y., ... & Hu, C. (2017). Embedding variable micro-capacitors in polydimethylsiloxane for enhancing output power of triboelectric nanogenerator. *Nano Research*, 10, 320-330. https://doi.org/10.1007/s12274-016-1294-4
- Xu, C., Zhang, B., Wang, A. C., Zou, H., Liu, G., Ding, W., ... & Wang, Z. L. (2019). Contact-electrification between two identical materials: curvature effect. ACS nano, 13(2), 2034-2041. https://doi.org/10.1021/acsnano.8b08533
- Xu, C., Zhang, B., Wang, A. C., Zou, H., Liu, G., Ding, W., ... & Wang, Z. L. (2019). Contact-electrification between two identical materials:

- curvature effect. *ACS nano*, *13*(2), 2034-2041. https://doi.org/10.1021/acsnano.8b08533
- Y Mi, X. Jing, Q. Zheng, L. Fang, H.-X Huang, L.-s. Turng, et al, Nonenergy **2018**, 48327-336. https://doi.org/10.1016/j.nanoen.2017.08.035
- Yao, C., Hernandez, A., Yu, Y., Cai, Z., & Wang, X. (2016). Triboelectric nanogenerators and power-boards from cellulose nanofibrils and recycled materials. *Nano Energy*, *30*, 103-108. https://doi.org/10.1016/j.nanoen.2016.09.036
- Yao, C., Yin, X., Yu, Y., Cai, Z., & Wang, X. (2017). Chemically functionalized natural cellulose materials for effective triboelectric nanogenerator development. *Advanced Functional Materials*, 27(30), 1700794. https://doi.org/10.1002/adfm.201700794
- Yao, C., Yin, X., Yu, Y., Cai, Z., & Wang, X. (2017). Chemically functionalized natural cellulose materials for effective triboelectric nanogenerator development. *Advanced Functional Materials*, 27(30), 1700794. https://doi.org/10.1002/adfm.201700794
- Yu, Y., & Wang, X. (2016). Chemical modification of polymer surfaces for advanced triboelectric nanogenerator development. *Extreme Mechanics*Letters, 9, 514-530. https://doi.org/10.1016/j.eml.2016.02.019
- Zakani, B., Entezami, S., Grecov, D., Salem, H., & Sedaghat, A. (2022).
 Effect of ultrasonication on lubrication performance of cellulose nano-crystalline (CNC) suspensions as green lubricants. Carbohydrate Polymers, 282, 119084.
 https://doi.org/10.1016/j.carbpol.2021.119084
- Żenkiewicz, M. (2007). Methods for the calculation of surface free energy of solids. *Journal of Achievements in Materials and Manufacturing Engineering*, 24(1), 137-145.
- Zhang, L., Cai, H., Xu, L., Ji, L., Wang, D., Zheng, Y., ... & Wang, Z. L. (2022). Macro-superlubric triboelectric nanogenerator based on tribovoltaic effect. *Matter*, 5(5), 1532-1546. 10.1016/j.matt.2022.02.021
- Zhang, R., & Olin, H. (2020). Material choices for triboelectric nanogenerators: A critical review. *EcoMat*, 2(4), e12062. https://doi.org/10.1002/eom2.12062
- Zhao, Z., Zhou, L., Li, S., Liu, D., Li, Y., Gao, Y., ... & Wang, Z. L. (2021). Selection rules of triboelectric materials for direct-current triboelectric nanogenerator. *Nature communications*, *12*(1), 4686. https://doi.org/10.1038/s41467-021-25046-z
- Zheng, J., Wei, X., Li, Y., Dong, W., Li, X., Shiju, E., ... & Wen, J. (2021).

 Stretchable polyurethane composite foam triboelectric nanogenerator with tunable microwave absorption properties at elevated temperature. *Nano Energy*, 89, 106397. https://doi.org/10.1016/j.nanoen.2021.106397
- Zou, H., Zhang, Y., Guo, L., Wang, P., He, X., Dai, G., ... & Wang, Z. L. (2019). Quantifying the triboelectric series. Nature communications, 10(1), 1427. https://doi.org/10.1038/s41467-019-09461-x



© 2024. The Author(s). This article is an open access article distributed under the terms and conditions of the Creative Commons Attribution-ShareAlike 4.0 (CC BY-SA) International License (http://creativecommons.org/licenses/by-sa/4.0/)